

The Galactic Midplane Is Not a Plane: Implications for Dynamical Analysis with *Gaia* Data and Beyond

ANGUS BEANE,^{1,2} ROBYN SANDERSON,^{1,2} MELISSA K. NESS,^{1,3} KATHRYN V. JOHNSTON,³ DOUGLAS GRION FILHO,³
MORDECAI-MARK MAC LOW,^{1,4} DANIEL ANGLÉS-ALCÁZAR,¹ DAVID W. HOGG,^{5,6,1,7} AND CHERVIN F. P. LAPORTE^{8,*}

¹*Center for Computational Astrophysics, Flatiron Institute, 162 5th Ave., New York, NY 10010, USA*

²*Department of Physics & Astronomy, University of Pennsylvania, 209 South 33rd St., Philadelphia, PA 19104, USA*

³*Department of Astronomy, Columbia University, 550 W 120th St., New York, NY 10027, USA*

⁴*Department of Astrophysics, American Museum of Natural History, Central Park West at 79th St., New York, NY 10024, USA*

⁵*Center for Cosmology and Particle Physics, Department of Physics, New York University, 726 Broadway, New York, NY 10003, USA*

⁶*Center for Data Science, New York University, 60 Fifth Ave., New York, NY 10011, USA*

⁷*Max-Planck-Institut für Astronomie, Königstuhl 17, 69117 Heidelberg, Germany*

⁸*Department of Physics & Astronomy, University of Victoria, 3800 Finnerty Rd., Victoria, BC, V8P 4H1, Canada*

ABSTRACT

Stellar actions, computed for stars from their six-dimensional phase space measurements and an assumed Galactic potential, are used to label and distinguish orbits. In principle, actions have the attractive quality of being invariant and thus good labels of a star’s orbit. Such analyses are often used to interpret data from the *Gaia* mission. However, inaccurate measurements of the phase space position and uncertainties in the assumed Galactic potential induce an error in the computed action. We show that, in addition to these complications, a systematic bias in the phase space position induces a phase-dependence in the actions, which we interpret as a systematic error. An offset in the vertical position of ~ 15 pc for a thin disk orbit or ~ 120 pc for a thick disk orbit is sufficient to induce a 25 % systematic error in the vertical action J_z computed under the assumption of an axisymmetric potential. The induced error distribution is non-Gaussian and bimodal, with neither of the modes peaking on the null value. Furthermore, we show that the local midplane varies by ~ 100 pc at the Solar circle in Milky Way-mass cosmological zoom-in simulations from the FIRE project. From observations that the mean vertical velocity of the Milky Way disk varies by ~ 5 km/s with radius, we estimate that the true midplane variations are of order ~ 60 – 90 pc. Thus, current state-of-the-art action calculations — which assume the global and local midplanes are the same — are likely to include a systematic vertical offset depending on the volume considered. Variation in the local standard of rest induces similar issues. The variation of the midplane must be taken into account when performing dynamical modeling across the large regions of the disk accessible to *Gaia* and future missions.

Keywords: Galaxy: disk – Galaxy: evolution – Galaxy: kinematics and dynamics – Galaxy: structure – solar neighborhood – stars: kinematics and dynamics

1. INTRODUCTION

Our understanding of the Milky Way is currently undergoing a revolution as a result of *Gaia* Data Release 2 (DR2). Recent major discoveries include the remnants of a major merger (Koppelman et al. 2018; Helmi et al. 2018; Lancaster et al. 2018; Mackereth et al. 2019), a phase-space “spiral” in the solar neighborhood (Antoja

et al. 2018) possibly indicating either local substructure infall (Binney & Schönrich 2018; Laporte et al. 2018b) or bar buckling (Khoperskov et al. 2018), and a gap suggestive of perturbation by a dark matter substructure in the tidal stream GD1 (Price-Whelan & Bonaca 2018; Bonaca et al. 2018). These discoveries all indicate that the Milky Way’s stellar distribution, which demonstrably departs significantly from axisymmetry, is undergoing phase mixing and dynamical interactions across a range of spatial and temporal scales.

Underlying the quantitative analysis of many of the mechanisms at work that give rise to these signatures

Corresponding author: Angus Beane
abeane@sas.upenn.edu

* Simons Fellow

is the assumption of a global, axisymmetric Galactocentric coordinate system (Binney & Tremaine 2008) in which the Sun’s position (and therefore the origin of the coordinate system) can be defined and measured both precisely and accurately. This involves measuring the angular position of and distance to the Galactic center, the orientation of the Galactic plane, the height of the Sun above the Galactic midplane, and the local standard of rest (LSR). We review the observational efforts to measure these parameters in Section 3.

Once a Galactocentric coordinate system has been established and a six-dimensional (6D) phase space measurement of a star has been made, it is often desirable to convert this measurement into action space to concisely summarize its projected orbit, model the stellar distribution function, or find stars with similar dynamical properties. Actions are conserved quantities that describe the orbit of a star under the assumption of regular, bound orbits in a system where the equations of motion are separable in a particular coordinate system. They are the cyclical integral of the canonical momentum over its conjugate position:

$$J_i \equiv \frac{1}{2\pi} \oint_{\text{orbit}} p_i dx_i. \quad (1)$$

Under the assumption of axisymmetry, $i = R, z, \phi$ are the radial, vertical, and azimuthal coordinates respectively in a cylindrical coordinate system and the p_i are the conjugate momenta. In a slowly-evolving axisymmetric potential, these actions are invariant and $J_\phi \equiv L_z$, where L_z is the z -component of the angular momentum (Binney & Tremaine 2008; Sellwood 2014).

With the advent of 6D phase-space measurements over a relatively large ($\gtrsim 2$ kpc) volume from the *Gaia* satellite, the study of stars’ actions has gained new popularity. One reason is dimensionality reduction—an individual stellar orbit is concisely described by three actions, as opposed to six phase space coordinates. Second, under the assumption of a phase-mixed system, the dynamical properties of a population of stars should be uniquely a function of their actions and independent of the conjugate angles, allowing investigation of the relationship between *orbital* properties of stars and other intrinsic, and at least partially invariant, properties such as age or metallicity (Beane et al. 2018; Ting & Rix 2018; Sanders & Das 2018; Gandhi & Ness 2019; Das et al. 2019; Bland-Hawthorn et al. 2019). Actions also provide a convenient basis for constructing models of the stellar distribution function (e.g. Jeans 1915; Villumsen & Binney 1985; Trick et al. 2017), or for associating stars with similar dynamical properties (e.g. to determine membership in moving groups).

If the system being considered departs from axisymmetry in a significant and/or non-adiabatic way, the actions computed using an axisymmetric approximation to the true potential can exhibit cyclic dependence on the orbital phase (or time at which the star’s position and velocity are observed), large-scale migration, or diffusion from their initial values. In the Milky Way, stellar actions are expected to diffuse on short time scales due to scattering with gas clouds and to evolve on longer time scales in the case of orbits near resonances with spiral arms, bar(s), and other large scale perturbations (Sellwood 2014). For this reason, we and other authors have used actions to study stellar scattering in the Milky Way disk using the improved astrometry of *Gaia* DR2 and various age catalogues (Beane et al. 2018; Ting & Rix 2018). Actions have also been used to study different models of spiral structure in the Milky Way (Sellwood et al. 2019). Characteristics of the distribution of stars in the extended solar neighborhood in action space are discussed in Trick et al. (2019).

The transformation to action space is nonlinear in both the phase-space position and the potential, and requires relatively strong assumptions about the system’s symmetry. However, the Galactic potential is not strictly axisymmetric; with the vast improvement in the quality of phase-space measurements due to *Gaia*, this assumption appears increasingly inadequate (e.g. Antoja et al. 2018). Even if this assumption were close enough for many purposes, the parameters used in axisymmetric models may be inadequately constrained by current observations.

In this work we discuss how the imposition of a global axisymmetric coordinate system based on a local measurement of the midplane location and Galactocentric distance introduces systematic error in the computation of actions, especially for stars in the thin disk. Our main point is that the “local” Galactic midplane is not the same as the “global” Galactic midplane. For stars relatively far from the Sun, their local midplane location will not agree with our local midplane extrapolated onto their position due to relatively small-scale variations in the density of the gas and stellar distribution. Converting positions and velocities of more distant stars from a heliocentric to a Galactocentric coordinate system introduces a systematic bias in the z coordinate, and hence the actions computed for these stars. The further from the solar neighborhood the target star, the more likely the mismatch will result in large systematic uncertainty, especially in the vertical action J_z . A similar argument applies to any remaining uncertainty in measurements of the Galactocentric radius of the Sun and to variations in the LSR.

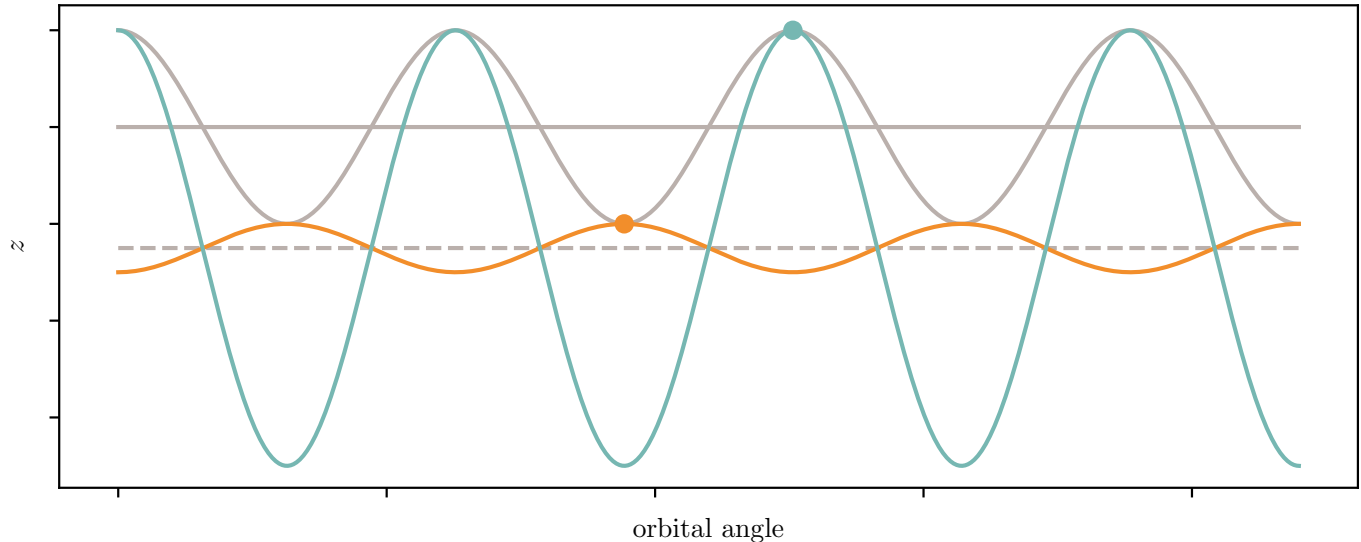


Figure 1. Cartoon approximation showing the effect an error in the determination of the coordinate midplane can have on orbit integration and action estimation. The x -axis shows the orbital phase and the y -axis the vertical height. The top gray curve depicts an example “true” orbit oscillating about the true midplane (horizontal solid gray line). Consider an observer who erroneously assumes the midplane is located at the horizontal dashed line. Suppose this observer measures the phase-space position of the star at two different orbital phases (teal and orange points). If the observer were then to integrate the star’s orbit using a model potential with the erroneous midplane, they would obtain the teal and orange curves for the star’s orbit, respectively. The actions estimated from these two erroneous orbits would subsequently differ, both from each other and from the actions estimated for the true orbit (in the potential with the correct midplane). Hence an incorrect midplane in the potential model assumed will induce phase-dependence in the actions estimated for a given star in that potential.

In Section 2, we describe the general impact coordinate system errors have on the measured actions. We then discuss two potential sources of these coordinate system offsets in Sections 3 and 4. In Section 3 we discuss the potential errors in measuring the parameters of the Galactocentric coordinate system. In Section 4 we examine the azimuthal variations of the midplane itself in two sets of simulations: cosmological, hydrodynamical, zoom-in simulations of Milky Way-mass galaxies from the Feedback in Realistic Environments (FIRE) collaboration¹ (Hopkins et al. 2014; Wetzel et al. 2016; Hopkins et al. 2018), and a controlled N-body simulation of a Sagittarius encounter with a galaxy otherwise tailored to the stellar mass, scale length, and scale height of the Milky Way (Laporte et al. 2018a).

In Section 5, we discuss the implications of midplane variations, and the resulting systematic uncertainty in the vertical action, for action-space analyses. We also estimate the expected midplane variations of the Milky Way based on the observed velocity variations. We summarize our main results and conclude in Section 6.

2. MOTIVATION

We first demonstrate the significance to action computations of a systematic offset in the determination of the Galactic midplane or distance to the Galactic center. We will find that such offsets are especially important for disk-like orbits. The consequences we explore here may also arise from various other systematic errors. For instance, the axisymmetric Galactic potential model used in many works to compute actions may not be a good description of the true potential — or the parameters used may yield a potential that is systematically incorrect outside an original fitted region. In this work, we assume that the Galaxy is perfectly described by our model axisymmetric potential, and simply explore the consequences of offsets in the determination of the Galactocentric coordinate system.

2.1. Effect of Midplane Offset

We present a cartoon approximation in Figure 1 to show how an inaccurate or erroneous determination of the midplane (and hence the zero-point of the z coordinate) leads to a phase-dependence of the actions calculated from an orbit specified by a phase-space point and an assumed potential model. The y -axis corresponds to the vertical height of the orbit and the x -axis shows orbital phase. The solid gray curve indicates the “true” orbit of the star; that is, its orbit as it oscillates around

¹ <https://fire.northwestern.edu>

the true midplane. The dashed gray line is the midplane location in the potential model used by an observer to integrate the orbit of the star and hence estimate its actions, which is offset from the true midplane of the star's orbit. The model potential is otherwise identical to the one in which the star is actually moving.

Now suppose this observer makes a measurement of the star's position and velocity at the teal point or the orange point (i.e. at two different orbital phases). Then the teal and orange curves correspond to the orbits that the observer would compute for each point based on the potential model with the offset midplane. In action space, this would correspond to a different value of J_z for the teal and orange points. In this way, assuming the wrong coordinate system induces a phase-dependence in the actions estimated for the star, which in the correct potential (in this example, the one with the correct midplane) should be phase-independent.

2.2. Epicyclic Approximation

Before turning to numerical methods, we first write down analytically the systematic error in the actions induced from either a midplane offset or a Galactocentric radius offset. We use the epicyclic approximation, which assumes that the motion in the z and R components of the orbit are decoupled and follow simple harmonic motion about a circular and planar “guiding orbit” (Binney & Tremaine 2008, Section 3.2 and references therein). We refer to the radius of this orbit (the “guiding radius”) as R_g . This approximation is an excellent description of thin disk-like orbits and a good description of thick disk-like orbits in an axisymmetric potential (i.e. ignoring the influence of the Galactic bar and spiral arms). We also make the assumption of a perfectly flat circular velocity curve with velocity v_c , a good approximation near the Solar circle (e.g. McMillan 2017).

Under this approximation, we can write down the cylindrical components of the orbits as

$$\begin{aligned}\phi(t) &= \Omega_c t \\ R(t) &= R_g + A_R \sin(\kappa t + \alpha) \\ z(t) &= A_z \sin(\nu t + \beta),\end{aligned}\tag{2}$$

where κ and ν are the radial and vertical frequencies, $\Omega_c \equiv v_c/R_g$ is the rotation frequency, A_z and A_R are the amplitudes of the stellar motion in the vertical and radial coordinates, and α and β are arbitrary constants. Similarly, the velocities of the orbit are given by:

$$\begin{aligned}v_\phi(t) &= v_c \\ v_R(t) &= \kappa A_R \cos(\kappa t + \alpha) \\ v_z(t) &= \nu A_z \cos(\nu t + \beta).\end{aligned}\tag{3}$$

In this case, we have that for J_ϕ (Binney & Tremaine 2008, Section 3.5.3b):

$$J_\phi = R_g v_c,\tag{4}$$

and for J_R and J_z :

$$\begin{aligned}J_R &= \frac{E_R}{\kappa} \\ J_z &= \frac{E_z}{\nu},\end{aligned}\tag{5}$$

where E_R and E_z are the energy per unit mass in the radial and vertical coordinates, respectively. Therefore,

$$\begin{aligned}J_R &= \frac{v_R^2 + \kappa^2(R - R_g)^2}{2\kappa} \\ J_z &= \frac{v_z^2 + \nu^2 z^2}{2\nu}.\end{aligned}\tag{6}$$

Using Equations (2) and (3), we can simplify this and write

$$\begin{aligned}J_R &= \frac{\kappa A_R^2}{2} = \frac{v_{R,\max}^2}{2\kappa} \\ J_z &= \frac{\nu A_z^2}{2} = \frac{v_{z,\max}^2}{2\nu},\end{aligned}\tag{7}$$

where the last equality in each line comes from the fact that $v_{R,\max} = \kappa A_R$ and $v_{z,\max} = \nu A_z$.

Notice that while the value for each of J_ϕ , J_R , and J_z is phase independent, the contribution from the kinetic and potential terms in Equation (6) is phase dependent. Now assume that the coordinates (R, z, v_ϕ, v_R, v_z) are offset by $(\Delta R, \Delta z, \Delta v_\phi, \Delta v_R, \Delta v_z)$. We can then apply the standard propagation of errors formula to Equation (6) to determine the error in each of the actions. For J_ϕ , the induced error is:

$$\frac{\Delta J_\phi}{J_\phi} = \frac{\Delta R}{R_g} + \frac{\Delta v_\phi}{v_c}.\tag{8}$$

For J_R , the induced error is:

$$\frac{\Delta J_R}{J_R} = \frac{2(R - R_g)}{A_R^2} \Delta R + \frac{2v_R}{v_{R,\max}^2} \Delta v_R.\tag{9}$$

For J_z , the induced error is:

$$\frac{\Delta J_z}{J_z} = \frac{2z}{A_z^2} \Delta z + \frac{2v_z}{v_{z,\max}^2} \Delta v_z.\tag{10}$$

We have ignored second order contributions.

Since most of the time stars will be at maximum amplitude (i.e. turnaround) in both R and z , we can approximate the order of magnitude of the systematic error

Table 1. Description and names of the three orbits considered in this work. For the last two columns: z_{\max} is the maximum height of the orbit while $\frac{1}{2}(R_{\max} - R_{\min})$ is the magnitude of the radial excursions of the orbit. In the epicyclic approximation, $A_z = z_{\max}$ and $A_R = \frac{1}{2}(R_{\max} - R_{\min})$.

name	initial position	initial velocity	J_R	J_ϕ	J_z	z_{\max}	$\frac{1}{2}(R_{\max} - R_{\min})$
	kpc	km/s	kpc km s ⁻¹	kpc km s ⁻¹	kpc km s ⁻¹	kpc	kpc
thin-disk	(8, 0, 0)	(0, -190, 10)	40.3	-1520	0.69	0.12	1.29
thick-disk	(8, 0, 0)	(0, -190, 50)	32.5	-1520	23.0	0.85	1.19
halo	(8, 0, 0)	(0, -190, 190)	32.8	-1520	529.1	6.16	2.34

in the actions by

$$\begin{aligned}
 \frac{\Delta J_\phi}{J_\phi} &= \frac{\Delta R}{R_g} + \frac{\Delta v_\phi}{v_c} \\
 \frac{\Delta J_R}{J_R} &= \frac{2\Delta R}{A_R} \\
 \frac{\Delta J_z}{J_z} &= \frac{2\Delta z}{A_z},
 \end{aligned} \tag{11}$$

where we have also ignored second order terms.

In the remainder of this section, we compare our analytic estimates of the effect of a midplane offset on actions against numerical calculations. A numerical evaluation of the effect of velocity offsets on actions is deferred to future work, as we discuss in Section 4.4.

2.3. Numerical Methods

We now quantify the argument made in Section 2.1 using numerical computations of the actions for a range of orbits in a model Galactic potential. We compute actions as in Beane et al. (2018), using the code `gala` v0.3 to perform orbit integrations and conversion to action space (Price-Whelan 2017; Price-Whelan et al. 2018). To compute actions we use the torus-mapping technique first presented by McGill & Binney (1990) and adapted by Sanders & Binney (2014) to calculate actions for an orbital time-series starting from a phase-space position (x, v) and integrated in a potential Φ . We use the default `MWPotential` as our potential, which is based on the Milky Way potential available in `galpy` (Bovy 2015). This potential includes a Hernquist bulge and nucleus (Hernquist 1990), a Miyamoto–Nagai disk (Miyamoto & Nagai 1975), and an NFW halo (Navarro et al. 1997), and is fit to empirically match some observations. We use the Dormand-Prince 8(5,3) integration scheme (Dormand & Prince 1980) with a timestep of 1 Myr and integrate for 5 Gyr, corresponding to ~ 20 orbits for a Sun-like star.

We assume the Sun is located at (8.2, 0, 0) kpc. None of our orbit calculations depend on the value of the LSR in this toy potential (though this is important when

using real data, since the conversion from heliocentric to Galactocentric coordinates depends on the LSR). In this potential, we have that the circular velocity v_{circ} is 231 km/s at the Solar circle.

Other methods for computing actions are used in the literature. For example, the Stäckel Fudge method (Sanders & Binney 2016), which uses a single Stäckel potential (with analytic actions) to approximate the Galactic potential (de Zeeuw 1985; Binney 2012), was used in many recent works exploring actions in the Galactic disk (e.g. Trick et al. 2019; Sanders & Das 2018; Ting & Rix 2018). For disk-like orbits, existing implementations of the Stäckel Fudge method are of acceptable accuracy, but since we also consider halo-like orbits in this work (where the Stäckel Fudge method is inaccurate) we choose to use orbit integration and torus mapping throughout (Sanders & Binney 2016).

2.4. Quantification of the Midplane Effect

We quantify how a systematic error in the Galactocentric coordinate system induces phase-dependence in the *observed* actions. We will consider three orbits in the model potential described in Section 2.3 that are typical of stars in the stellar thin disk, stellar thick disk, and the stellar halo. We summarize their initial positions in phase space and the actions computed by integrating their orbits in the correct potential in Table 1. Each orbit, integrated without systematic coordinate errors, is plotted in Appendix A. We will refer to these orbits by their names (thin-disk, thick-disk, halo) henceforth.

We begin with the thick-disk orbit. Consider an immortal observer who can measure the thick-disk star’s phase-space position at many different times (and hence different orbital phases). However, the immortal observer uses a coordinate system in which the midplane is systematically offset in height by 100 pc from its actual location — i.e. we subtract the vector (0, 0, 100) pc from each position in the orbit. This corresponds to the immortal observer physically located at e.g. the position (8, 0, 0) kpc in the coordinate system of the true

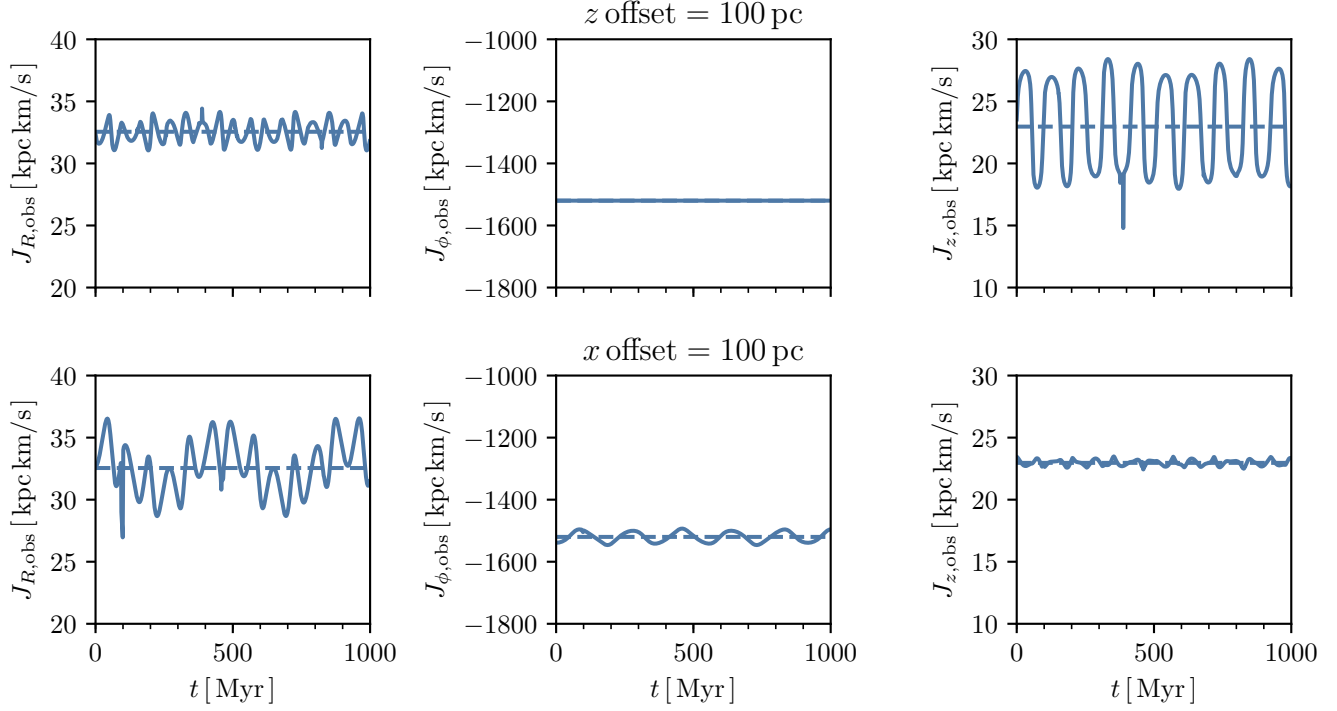


Figure 2. The artificial phase-dependence in the observed actions induced by an error in the Galactocentric coordinate system. We consider here the thick-disk orbit, which has actions of $(J_R, J_\phi, J_z) = (37.9, -1520, 7.0)$ kpc km/s and $z_{\max} = 850$ pc (see Table 1). We integrate the orbit according to the procedure laid out in Section 2.3, and which we plot in Appendix A. Then, we subtract 100 pc from the z value (upper panels) or the x value (lower panels) of each position in the orbit, corresponding to an erroneous observer assuming a midplane (upper) or solar radius (lower) that is off by 100 pc. We then allow an immortal observer to observe the orbit over 1 Gyr and perform the same orbit integration procedure at each timestep, and report the values of the actions. The computation of J_ϕ is pristine to errors in z , with only numerical artifacts remaining. Only small errors are induced in J_R , with the middle 90% of values over the Gyr being within $\sim 8\%$ of the true J_R . As expected, large errors are induced in J_z with a 100 pc offset in z , with the middle 90% of values being within $\sim 43\%$ of the true J_z . The x offset induces uncertainties in J_R , J_ϕ , and J_z of $\sim 21\%$, $\sim 3\%$, and $\sim 3\%$.

potential, but erroneously thinking they are located at $(8, 0, 0.1)$ kpc.

We consider that the immortal observer makes a measurement every Myr. At each measurement, we compute the actions as outlined above using the true potential but by specifying the star’s starting position using the systematically offset coordinate system. Essentially we are shifting the integrated orbit and then reintegrating at each point along the shifted orbit, where the shifted orbit is the observed orbit. The erroneous computed actions for each phase-space starting point are shown for the first Gyr of the orbit in the upper panels Figure 2.²

² Occasionally the numerical scheme fails and very large actions are reported by `gala`—we perform a 5σ clip on each action to exclude such orbits, but this only excludes a total of 5 orbits out of the 1000 considered for Figure 2. Some numerical artifacts remain, but the vast majority of orbits are computed properly.

We also perform the same procedure but assume a 100 pc offset in the x component (i.e. subtracting the vector $(100, 0, 0)$ pc) in the lower panels. This is equivalent to a systematic offset in the determination of the distance from the Sun to the Galactic center.

Figure 2 shows that the actions computed in the offset coordinate systems depend on the time (i.e. orbital phase) at which the star’s phase-space position is observed. To the immortal observer this would appear as time-dependence in the actions, which appear to oscillate around their value using the correct coordinate system even though in this example the observer is using the correctly constructed best-fit static, axisymmetric potential. The relative size of the phase variation in each action depends on the direction of the systematic offset as well as the true values of the actions (i.e. the type of orbit). In reality we will have one measurement of the phase-space position to work with, in which case the de-

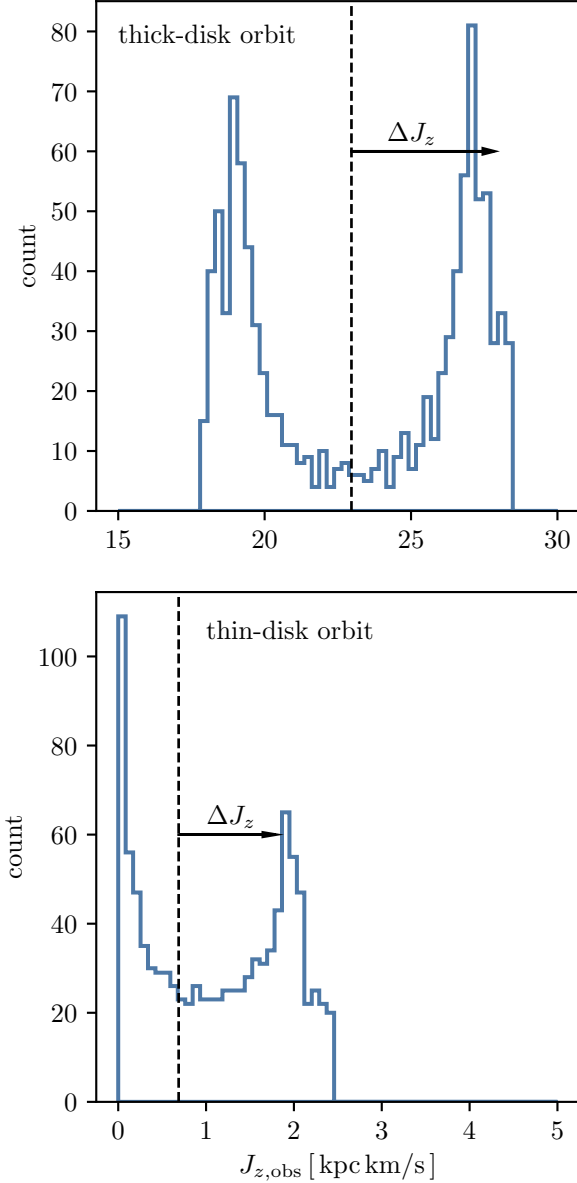


Figure 3. A histogram of the observed values in J_z for the thick-disk (top panel) and thin-disk (bottom panel) orbits assuming a z offset of 100 pc. One can see that if the observed z values have a bias (from e.g. an incorrectly computed midplane), then the induced error distribution in J_z is decidedly non-Gaussian. Therefore, any sort of error propagation must take this into account. Intuition for the shape of each panel is given in the text. We also plot one half the 95th percentile minus the 5th percentile of each distribution as a horizontal arrow anchored on the true J_z value. We call this ΔJ_z and will use it (along with the similarly defined ΔJ_R and ΔJ_ϕ) to empirically describe the error distribution. We see that ΔJ_z roughly corresponds to the distance from the true J_z value to one of the modes of the distribution of observed J_z values. Similar plots for J_R induced by a z offset and J_R and J_ϕ induced by an x offset are given in Appendix C.

termination of the orbital phase in R or z is degenerate with the degree of systematic offset in that coordinate (see Figure 1). In the following we therefore quote percentile ranges for the possible values computed for each action as a proxy for the effect of these systematic errors in the coordinate system.

For a systematic offset in z (upper panels), the 95th minus 5th percentiles are 2.2 and 6.2 kpc km/s for J_R and J_z , respectively. These are fractional errors of 5.7% and 86%, respectively. The error induced in J_ϕ is negligible, as expected since J_ϕ only depends on the x - and y -components of the position and velocity of the stars.³ It is worth pointing out that a 100 pc error in an orbit with $z_{\max} = 850$ pc — a 12% error — induced an 86% error in the computation of J_z .

For a systematic offset in x (or distance to the Galactic center), the 95th minus 5th percentiles are 6.9, 47, and 0.71 kpc km/s for J_R , J_ϕ and J_z , respectively. These are fractional errors of 21%, 3.1% and 3.1%, respectively — despite only a 1.2% error in the distance to the Galactic center.

In Figure 3 we plot a histogram of the observed values of J_z for the thick-disk orbit (top panel) and thin-disk orbit (bottom panel) assuming a z offset of 100 pc (i.e. as in the upper right panel of Figure 2). The true value of J_z is plotted as a vertical dashed line. Here we see that the errors in J_z induced by a systematic offset in z are non-Gaussian and bimodal. Furthermore, neither of the modes lie at zero. In other words, neither of the modes of the distribution of observed J_z values are centered on the true J_z (i.e. the J_z computed with no offset in z). In the case of the thin-disk orbit (bottom panel), we see that, in addition to the prior complications, the error distribution is not even centered on null. This comes about when the midplane error is $\gtrsim z_{\max}$, where z_{\max} is the maximum height of the orbit, equivalent to A_z in the epicyclic approximation (see Section 2.2).

In Appendix C we plot the same histogram as in Figure 3, but for the observed distributions of J_R induced by a z offset (upper left panel of Figure 4) and the observed distributions of J_R and J_ϕ errors induced by an x offset (lower left and lower center panels of Figure 4, respectively). We find similar error distributions as in Figure 3, with the exception that the observed J_R distribution induced by an x offset more closely resembles a Gaussian.

We now describe the intuition behind the shape of Figure 3. Consider first the thick-disk orbit (top panel), where the offset in z is much less than z_{\max} of the orbit.

³ In practice, however, J_ϕ is computed as part of the torus-fitting method.

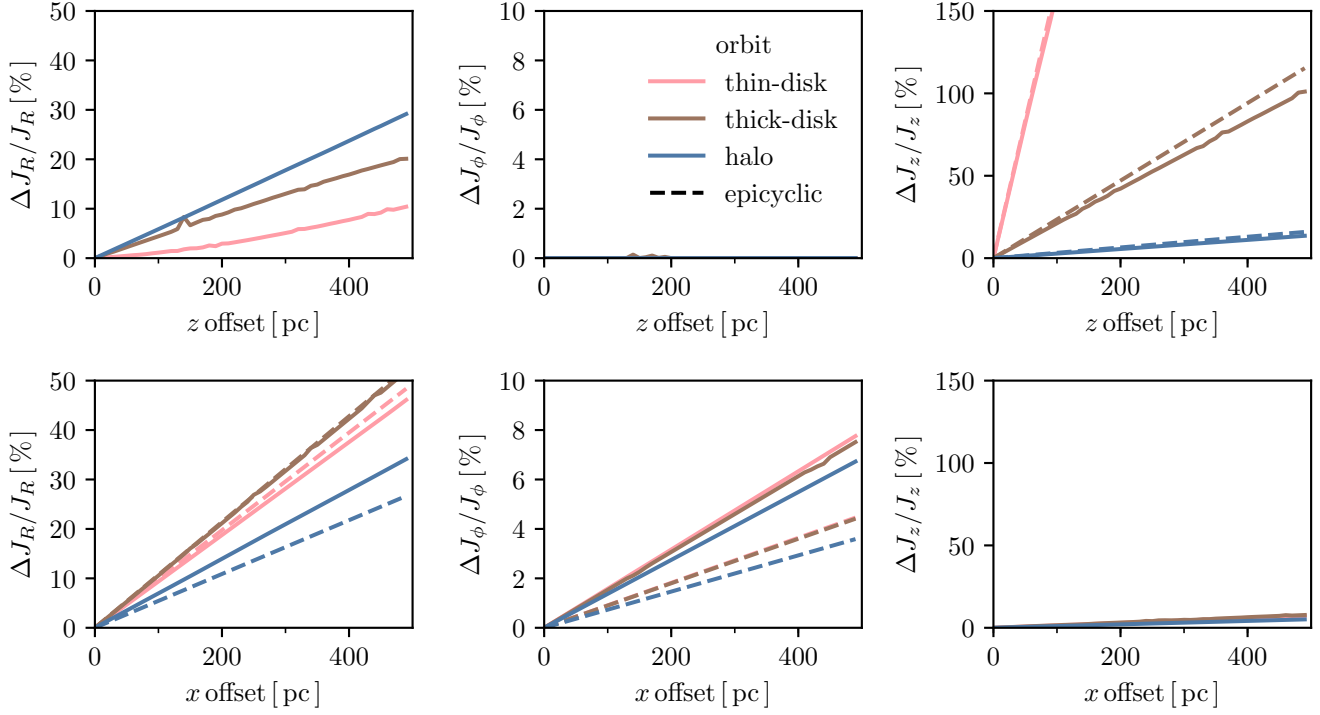


Figure 4. We report one half the 95th minus 5th percentile of the error in the measured action (ΔJ_i) from coordinate system errors for the thin, thick, and halo orbits (Table 1). See discussion in the text for the justification in using this to measure the magnitude of the induced error. The left, center, and right panels show the result for J_R , J_ϕ , and J_z , respectively. The upper panels consider an offset in z and the lower panels consider an offset in x (equivalently, an offset in the Solar radius). In some panels we also plot as dashed lines the epicyclic prediction of the induced action error (Equation (11)). In the epicyclic approximation, a z offset only induces an error in J_z — for all three orbits the epicyclic approximation is a good description of the J_z error. An x offset induces an error in J_R and J_ϕ . The error in J_R is somewhat well-described for the thin-disk and thick-disk orbits, and a poor description for the halo orbit. For J_ϕ , the epicyclic approximation is not a good description for any orbit.

The peaks in the distribution correspond to the turning points of the orbit (or points of maximum vertical amplitude), where $v_z \sim 0$ and where the star is on most of its orbit. This is why the distribution is peaked on these values. For the thin-disk orbit (bottom panel), the offset in z is comparable to z_{\max} . Now, there will be some points in the orbit where $v_z = 0$ and $z = 0$ (in the observed, erroneous coordinate system). At these points, the computed J_z will vanish. The asymmetry and systematic offset then comes about because of the constraint that $J_z \geq 0$.⁴

Empirically describing the error distribution shown in Figure 3 is difficult. Of course, Gaussian summary statistics are not adequate. We therefore elect to measure this error by computing one half the 95th percentile

minus the 5th percentile of the distribution of observed action values. We refer to this quantity as ΔJ_i for each action value. We plot this quantity in Figure 3 as a horizontal arrow anchored on the true action value. Because of the bimodality of the error distribution, this quantity roughly measures the distance from the true action value to the peak of one of the modes. Furthermore, this bimodality also implies that ΔJ_i is not very sensitive to the exact percentiles used. This summary statistic does not reflect the bias induced when the midplane error is $\gtrsim z_{\max}$.

We now repeat the same procedure as in Figure 2 but for systematic offsets between 0 and 500 pc in the z and x components. In Figure 4, we report one half the 95th minus 5th percentile divided by the true action value ($\Delta J_i/J_i$) for the three different fiducial orbits in Table 1. The thick-disk (brown) orbit is the one from Figure 2, but we also now consider the effect on the action determined for the thin-disk (pink) and halo (blue) orbits.

⁴ This is similar to arguments in cosmology for why gravity produces non-Gaussianity in the density field, since the density cannot become negative but it can grow arbitrarily large.

The upper row of Figure 4 shows the spread induced in each action for an offset in the z -component (i.e. the Galactic midplane). In the lower row we consider offsets in the x component (i.e. the Solar radius). The left, center, and right columns show the fractional spread in the values computed for J_z , J_ϕ , and J_R , respectively. We compute the fractional spread $\Delta J_i/J_i$, where ΔJ_i is defined in the previous paragraph and J_i is the action value computed in the true coordinate system, over the course of the first Gyr.

In the upper middle panel of Figure 4, there is essentially no spread in the determination of J_ϕ . This is expected since J_ϕ is independent of z and is thus unaffected by offsets in z , as discussed earlier. Indeed, the result we found in Figure 2 for the thick-disk orbit holds for all orbit types. This is also a demonstration of the robustness of the orbit integration and action calculation methods we use.

The upper right panel of Figure 4 shows that the fractional error in J_z is more exaggerated for more planar (disk-like) orbits. For the thin-disk orbit, a systematic offset of ~ 15 pc in the z coordinate already results in 25% deviations in the actions. The required offset for 25% deviation is ~ 120 pc for the thick-disk orbit. The halo orbit is relatively resistant to errors in the midplane, with only $\sim 15\%$ error in J_z out to a midplane offset of 500 pc.

For the offset in the Solar radius (lower panels), the error is largest for J_R , with some deviations resulting in J_ϕ and relatively small deviations in J_z . In the lower middle and lower right panels all three lines nearly overlap.

In each panel of Figure 4, where relevant, we include the estimation of the action errors derived under the epicyclic approximation from Equation (11), with $\Delta v_\phi = 0$, as dashed lines in the color of each orbit. This equation is relevant since during most of the orbit the star will be at maximum radial and vertical amplitude and we do not consider velocity offsets. Note that we consider an error in the x -coordinate Δx , which is not exactly the same as ΔR . For observations of stars close to us, we have that $\Delta x \sim \Delta R$, but for the experiment performed in this Section we consider observations of the star throughout its entire orbit. This introduces a factor of $2/\pi$ when converting from Δx to ΔR , which we derive in Appendix B.

The epicyclic approximation is a good predictor of ΔJ_z , even for halo orbits. It performs similarly for ΔJ_R , now underpredicting for halo orbits and slightly overpredicting for thin-disk orbits. Note that for the particular orbits we chose, the thin-disk orbit has slightly larger A_R than the thick-disk orbit, and so we expect the epicyclic

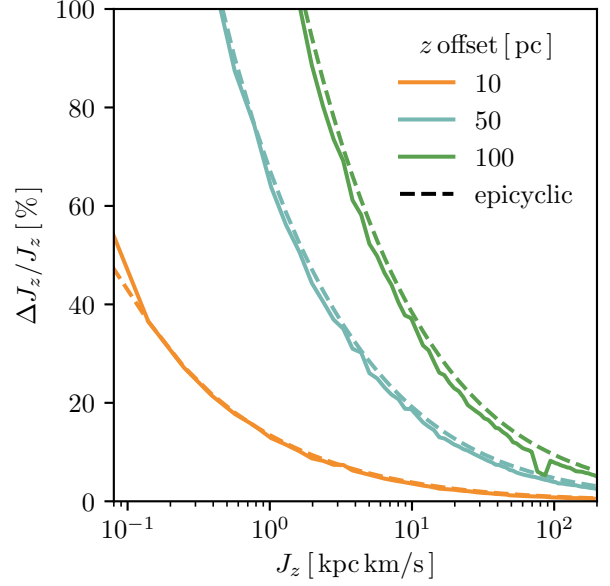


Figure 5. The fractional error in J_z as a function of J_z for a few different offsets in z . All orbits have the same initial position of $(8, 0, 0)$ kpc and velocity $(-190, 0, v_z)$ km/s, where we vary v_z . We show this for a z offset of 10, 50, 100 pc (orange, teal, and green respectively). As before, the error (ΔJ_z) is one half the 95th minus 5th percentile of the distribution of observed J_z values over the course of the orbit. There are large errors for thin-disk like orbits ($J_z \sim 0.5$ kpc km/s), even for a small midplane offset of 10 pc. As dashed lines in each color we also plot the prediction for $\Delta J_z/J_z$ from the epicyclic approximation (Equation (11)), which shows excellent agreement with the numerically computed values.

approximation to perform slightly worse. The epicyclic approximation underpredicts ΔJ_ϕ for all orbits.

To further understand the effect of the midplane error, we also plot the fractional error in J_z as a function of J_z for z offsets of 10, 50, 100 pc (orange, teal, and green, respectively) in Figure 5. For each orbit, we set the initial position to be $(8, 0, 0)$ kpc and the initial velocity to be $(-190, 0, v_z)$ km/s, where we vary v_z . For a thin disk-like orbit ($J_z \sim 0.5$ kpc km/s), even a 10 pc offset in z is enough to induce a $\sim 25\%$ error in J_z . For larger values of J_z , the fractional errors are suppressed, but the induced error can still be large depending on how great the z offset is. We also plot the epicyclic prediction for $\Delta J_z/J_z$ from Equation (11) as dashed lines for each z offset. We find that the epicyclic approximation matches the numerical estimate quite well.

3. COORDINATE SYSTEM OFFSETS I. MEASUREMENT ERRORS

We consider the first potential source of coordinate system offsets which would generate the action errors described in Section 2: uncertainties in measurements of the position and velocity of the Sun relative to the Galactic center. Converting from heliocentric to Galactocentric coordinates relies on these measurements. Therefore, errors in their values will induce a systematic offset in the Galactocentric phase-space position of any observed star.

3.1. Galactic Center

First, one must define the center of the Galaxy. This is usually taken to be the location of the central super-massive black hole, Sagittarius A* (Sgr A*, e.g. Reid & Brunthaler 2004). From stellar motions near Sgr A*, the distance from the Sun to Sgr A*, referred to as R_0 , can be precisely measured (Gillessen et al. 2009; Gravity Collaboration et al. 2018), with a recent measurement using near-infrared interferometry of 8.178 ± 0.035 kpc (Abuter et al. 2019).

3.2. Galactic Orientation

Second, one must define the angular orientation of the Galaxy. This was defined in 1958 by the IAU sub-commission 33b (Blaauw et al. 1960) by defining the coordinates of the Galactic center in B1950 coordinates as (17:42:26.6, -28:55:00) and the North Galactic pole as (12:49:00, +27:24:00). These two quantities, together with R_0 , define the orientation of the Galactic plane. However, there is growing evidence that the stellar midplane is tilted relative to this coordinate system (Goodman et al. 2014; Bland-Hawthorn & Gerhard 2016), though not the H II midplane (Anderson et al. 2019).

3.3. Solar Height

Third, one must define the Sun’s vertical distance from the Galactic midplane, which can be determined by identifying where the stellar density and velocities reach a maximum (effectively the median height of all disk stars). The Solar height is usually taken to be ~ 25 pc (Chen et al. 2001), with a more recent measurement from *Gaia* DR2 placing it at 20.8 ± 0.3 pc (Bennett & Bovy 2019). Another strategy is to use the cold gas or H II regions in the disk to define the Galactic midplane, leading to slightly different values (by ~ 5 pc) for the Sun’s relative height (e.g. Anderson et al. 2019). A pre-*Gaia* review of these measurements is given by Bland-Hawthorn & Gerhard (2016).

3.4. Local Standard of Rest

Finally, one must define the LSR, or mean velocity of stars near the Sun relative to the Galactic center

(which is defined to have zero velocity), and the velocity of the Sun relative to the LSR. The radial (U_\odot) and vertical (W_\odot) components are computed by taking the mean motions of different stellar groups (e.g. Schönrich 2012). The azimuthal component (V_\odot) is more difficult to measure, but can be modeled using the asymmetric drift relation (Binney & Tremaine 2008). The values of the components of the LSR are usually taken from Schönrich et al. (2010). The value of the circular velocity is taken to be ~ 220 km/s (e.g. Bovy et al. 2012).

Considerable effort has been placed on each of these measurements, but uncertainties remain, and detailed dynamical modeling across the disk — particularly for dynamically cold stars — may have to take them into account. For instance, the discrepancy of ~ 5 pc between the midplane defined by stars and by gas will induce a $\sim 10\%$ error in J_z for an orbit with $z_{\max} \sim 100$ pc (see Section 2).

4. COORDINATE SYSTEM OFFSETS II. AZIMUTHAL MIDPLANE VARIATIONS IN SIMULATIONS

We now consider a second source of systematic offsets in the Galactocentric coordinate system: intrinsic variations of the midplane across the disk. In this work we specifically consider azimuthal variations in the midplane as defined by the stellar mass density. We use two sets of simulations of Milky Way-mass galaxies to estimate the size of this effect.

4.1. Description of FIRE Simulations

The FIRE cosmological hydrodynamic simulations (Hopkins et al. 2014, 2018) use the zoom-in technique (e.g. Katz & White 1993; Oñorbe et al. 2014) to model the formation of a small group of galaxies at high resolution in a full cosmological context. Feedback from supernovae, stellar winds, and radiation from massive stars is implemented at the scale of star forming regions following stellar population synthesis models, generating galactic winds self-consistently (Muratov et al. 2015; Anglés-Alcázar et al. 2017) while reproducing many observed galaxy properties, including stellar masses, star formation histories, metallicities, and morphologies and kinematics of thin and thick disks (Hopkins et al. 2014; Ma et al. 2016, 2017; Wetzel et al. 2016; Garrison-Kimmel et al. 2018; Hopkins et al. 2018). For this work, we focus on the three Milky Way-mass zoom-ins considered in Sanderson et al. (2018), which were simulated as part of the *Latte* suite and show broad agreement of many of their global properties with observations of the Milky Way (Wetzel et al. 2016; Garrison-Kimmel et al.

2018). The $z_r = 0$ snapshots⁵ of these three simulations, named **m12i**, **m12f**, and **m12m** for shorthand, are publicly available alongside associated mock *Gaia* DR2 catalogues generated from them.⁶

These simulations contain dark matter particles of mass $\sim 35,000 M_\odot$, gas particles of mass ~ 7000 to $20,000 M_\odot$, and star particles of mass ~ 5000 – $7000 M_\odot$, with the lower end coming from stellar evolution (Sanderson et al. 2018). Softening lengths for dark matter and star particles are fixed at 112 pc and 11.2 pc, respectively.⁷ The gas softening length is adaptive, but at $z_r = 0$ the median softening length for cold ($T < 10^4$ K) gas particles around roughly solar positions (with galactocentric cylindrical radii within 0.5 kpc of 8.2 kpc and $|z| < 1$ kpc) is 12.4, 12.5, and 10.3 pc for **m12i**, **m12f**, and **m12m**, respectively. These values are summarized in Table 2, along with measurements of the stellar and gas disk scale heights.

The softening lengths used in the simulations can affect the ability to resolve the very thinnest planar structures, which in turn can affect how much the density-based midplane varies as a function of azimuth. The Milky Way’s dense, star-forming gas disk is thought to have a scale height of about 40 pc, ~ 3 – 4 times the cold gas softening length (Anderson et al. 2019). The thin stellar disk has a scale height of about 300 pc, ~ 30 times the stellar softening length (Jurić et al. 2008). We therefore expect that resolution effects may still be affecting the scale heights of these components in the simulations, especially the cold gas. Indeed, the stellar scale heights of the simulated galaxies are equal to or larger than the Milky Way’s while the gas scale heights are significantly larger (although the proper basis comparison is less clear in the case of the gas; the quoted value for the Milky Way comes from studies of high-mass star-forming regions). As noted above, the midplanes defined by gas and stars can be tilted with respect to one another as well, precluding extending the precision of the gas midplane definition to the stellar component.

Cosmological simulations of Milky Way-mass galaxies are not perfect representations of the true Milky Way in other ways as well,⁸ as discussed in Sanderson et al. (2018). For instance, the velocity structure of **m12i** is

closer to M31’s than the Milky Way’s (Loebman et al. in prep). However, in this work we are most interested in the global properties of the potential, and specifically in deviations from axisymmetry. From this perspective, the simulated galaxies are actually *more* axisymmetric than we might expect of the Milky Way. While they have prominent spiral arms, none has as strong a bar as the Milky Way does at present day, and none has a nearby companion like the Large Magellanic Cloud. One of the three we consider (**m12f**) does have an ongoing interaction with a satellite galaxy similar to Sagittarius, which has punched through the galactic disk outside the solar circle and induced some warping.

In this work, we take the galactocentric coordinate system described in Section 3 of Sanderson et al. (2018) as our fiducial coordinate system for each galaxy. In short, the center of the galaxy is found iteratively. The center of mass velocity is then determined by all star particles within 15 kpc of this center. The galaxy is then rotated onto a principal axis frame determined by stars younger than 1 Gyr inside of the fiducial solar radius $R_0 = 8.2$ kpc, such that the disk plane is the x – y plane.

4.2. Description of Milky Way-Sagittarius Interaction Simulation

In addition to the cosmological zoom-ins, we will also briefly consider results from a toy Sagittarius encounter simulation. This simulation offers us the ability to see how the midplane varies in a more controlled environment. The details of the simulation are given in Laporte et al. (2018a), but we briefly summarize the most relevant details here. For the Milky Way, the dark halo is modeled as a Hernquist sphere of mass $10^{12} M_\odot$ and scale length of 52 kpc, the disk modeled as an exponential disk with a scale radius of 3.5 kpc, scale height 0.53 kpc, and mass $6 \times 10^{10} M_\odot$, a Hernquist bulge of mass $10^{10} M_\odot$ and scale length 0.7 kpc (Hernquist 1990). Sagittarius is modeled as a dark matter Hernquist sphere of mass **something** and scale length **something**, along with a stellar component modeled as a Hernquist sphere of mass $6.4 \times 10^8 M_\odot$ and scale radius 0.85 kpc. All components are realized with live distributions of N-body particles; the Milky Way and Sagittarius are each initialized to be in equilibrium in isolation **check!**.

The mass resolution of the simulation is 2.6×10^4 , 1.2×10^4 , and $1.0 \times 10^4 M_\odot$ for the dark matter, disk, and bulge components, respectively. For the disk and bulge components, a softening length of 30 pc is used whereas for the halo a softening length of 60 pc is used. For Sagittarius, the softening length for the dark matter and the stars is 60 and 40 pc, respectively.

⁵ In this work, to avoid confusion with the vertical height z , we refer to cosmological redshift as z_r .

⁶ <http://ananke.hub.yt>

⁷ This is 2.8 times the often-quoted Plummer-equivalent.

⁸ The failure of cosmological simulations to exactly reproduce the Milky Way is not entirely due to limitations of the numerical model. Candidate Milky Way-like galaxies are chosen solely on their mass and isolation, for which there are a wide variety of possible galaxies with qualitatively different properties.

Table 2. Stellar and gas disk scale heights of the real Milky Way and the simulated galaxies considered in this work. For comparison, we also give the softening lengths for the simulated galaxies.

galaxy	cold ^a gas disk	stellar thin disk	stellar thick disk	cold gas softening length	stellar softening length
	(pc)	(pc)	(pc)	(pc)	(pc)
Milky Way ^b	40	300	900
m12i ^c	800 ^d	480	2000	12.4	11.2
m12f ^c	360	440	1280	12.5	11.2
m12m ^c	250	290	1030	10.3	11.2

^a $T < 1000$ K

^bJurić et al. (2008); Bland-Hawthorn & Gerhard (2016)

^cSanderson et al. (2018)

^dThe azimuthally averaged gas vertical density profile in m12i is nearly constant to this height, though individual regions show smaller scale heights and dense clouds.

The fiducial coordinate system for these toy simulations is the rest frame of the aligned toy galaxy at the beginning of the simulation.

4.3. The Local Midplane

Using the two sets of simulations, we determine the local midplane that an observer might measure if they were situated in each of these galaxies as a function of azimuth at the solar circle. Starting from the coordinate system described in the previous section, which is approximately aligned so that the z -coordinate is perpendicular to the disk plane, we place our imaginary observer at $z = 0$ and a galactocentric cylindrical radius of 8.2 kpc and vary the azimuth between $0 < \phi < 2\pi$.⁹ At each value of ϕ we then compute the median z for stars within a cylinder of radius 0.5 kpc and height 1 kpc perpendicular to the fiducial disk. We then re-define the new midplane of the cylinder to be the median z , re-select stars, and iterate until the median z value converges. We find that only 10 iterations of this procedure are necessary for convergence. The resulting median z is taken to be what our observer would measure as the local Galactic midplane at each ϕ .

This procedure assumes perfect density estimation, and therefore perfect corrections for extinction within the cylinder defining the “solar neighborhood.” Imperfect extinction correction is likely to increase the amplitude of the estimated fluctuations in z .

⁹ The immortal observer also has warp drive, allowing them to travel around the galaxy much more quickly than its dynamical timescale (warp factor ~ 0.25). Using warp drive allows them to circumvent time dilation effects.

To account for the effect of particle noise, we bootstrap resample stars within a cylinder of stars with height 2 kpc and the same radius 1000 times and determine the 1σ error bars by repeating the midplane determination with those reselection of stars.

To allow for potential small inaccuracies in the determination of the original fiducial coordinate system, we also subtract the best fit $A \sin(\phi + B) + C$ curve from the midplane as a function of azimuth to account for an overall tilt of the midplane (a simplified version of the strategy described in Anderson et al. 2019). For A the values are -165 , 45 , and 8.8 pc, for B the values are 0.67 , -0.088 , and 0.031 rad and for C the values are -69 , 19 , and -18 pc for m12i, m12f, and m12m, respectively. For the assumed Solar radius of 8.2 kpc, we can approximate the angle offset for the z -axis from the values of A — we compute 1.15 , 0.31 , and 0.06 deg for m12i, m12f, and m12m. These angle offsets are consistent with the values given in Sanderson et al. (2018) for the difference between the z -axis as defined by the gas and stars.

Figure 6 shows the relative z location of the inferred midplane our imaginary observer would determine as a function of azimuth for each galaxy, using their local “solar neighborhood” (the cylinder defined above). We consider 50 equally spaced bins in azimuth, a sufficient number such that each cylinder shares no stars with its neighboring cylinder. The 1σ error from the bootstrap procedure is shown as the dashed-line error bars. The middle 90% of midplane values across the Solar circle spans 185, 162, 84 pc for m12i, m12f, and m12m. In two of the three cases the midplane therefore varies by more than ± 100 pc depending on the azimuth along the Solar circle; in the third (m12m, which has the thinnest “thin

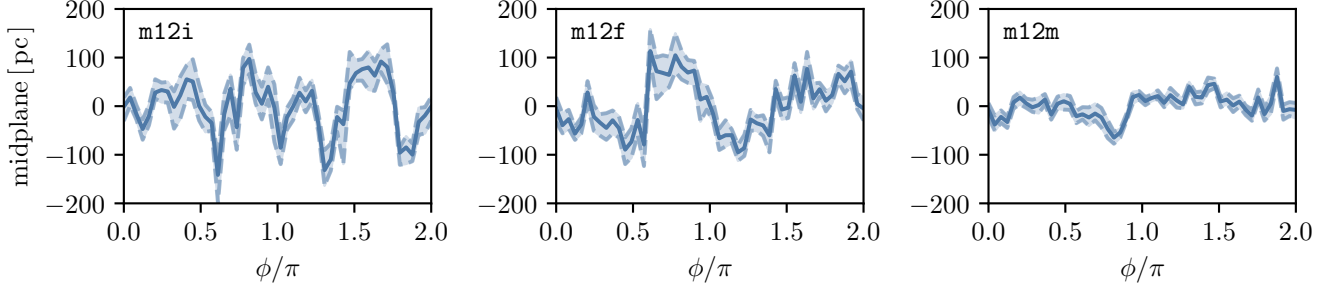


Figure 6. The local midplane determined at the fiducial Solar radius (8.2 kpc) for the three FIRE galaxies **m12i**, **m12f**, and **m12m** (left, center, and right panels) as a function of azimuthal angle. All calculations are done at cosmological redshift $z_r = 0$. The local midplane is determined at a position ϕ by taking the median height of all stars within $R = 0.5$ kpc and $z = 1$ kpc (in cylindrical coordinates). The procedure is performed again using the new height 10 times to converge on the local midplane height. In order to allow for the possibility that the fiducial galactocentric coordinate system is incorrect, we subtract the best fit $A \sin(\phi + B) + C$ curve from each panel — this figure is reproduced with the original midplane determination (i.e. before subtracting the best fit sine curve) in Appendix D. We then bootstrap resample 1000 times on all stars within a 2 kpc height of the fiducial midplane to determine 1σ error bars, which we report as dashed lines.

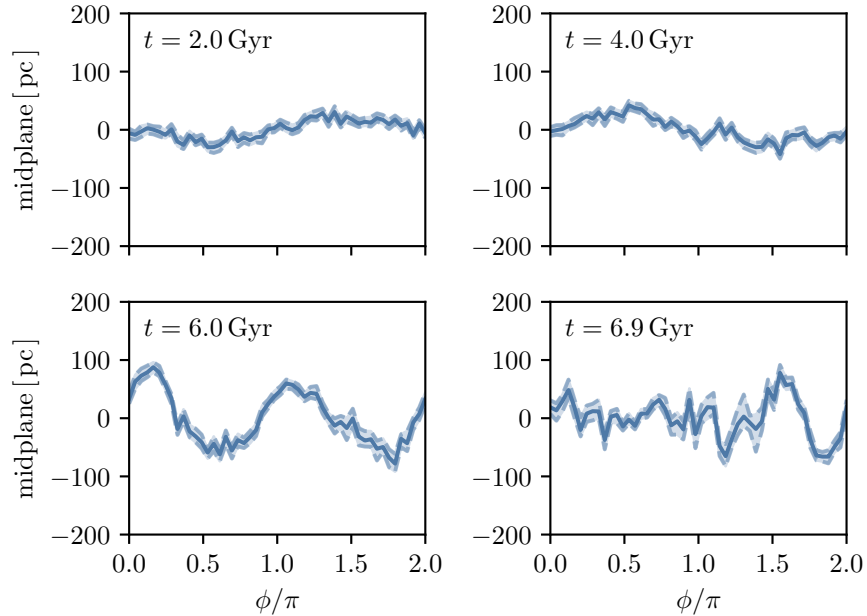


Figure 7. The local midplane determined at the fiducial Solar radius (8.2 kpc) for 4 different time steps from toy simulations of a Sagittarius encounter with the Milky Way (Laporte et al. 2018a). As before, we have subtracted the best fit $A \sin(\phi + B) + C$ curve to account for inaccuracies in the galactocentric coordinate system. Error bars are calculated as in Figure 6. (Check:) The upper panels show the midplane as a function of azimuth before the first encounter near the Solar circle at $t = 2.0$ Gyr and $t = 4.0$ Gyr. As later encounters occur which bring the Sagittarius-like object closer to the Solar circle, we can see that stronger midplane variations result. In fact, one can see that an $m = 2$ mode is excited in the lower left panel at $t = 6.0$ Gyr — this is consistent with Figure 17 of Laporte et al. (2018a), which shows that an $m = 2$ mode is excited (note that $m = 0$ and $m = 1$ modes are stronger, but these are removed in our sine-curve subtraction). The fact that the $t = 6.9$ Gyr panel looks qualitatively similar to the panels from the FIRE simulations (Figure 6) is evidence that the midplane variations are produced in part by mergers.

disk” of stars, but the largest stellar mass) the variation is closer to ± 50 pc.

We compute the same midplane variation in Figure 7, but for four successive timesteps of the toy simula-

tion of a Sagittarius encounter (Laporte et al. 2018a). Again we have subtracted a best fit curve of the form $A \sin(\phi + B) + C$, with the values for A being 9.5, 2.5, -212, and -394 pc, for B being 0.0013, 0.0007, -0.63, and -1.00 rad and C being 2.6, -7.8, -65, and -53 pc chronologically for each of the four timesteps shown.

In the upper panels, we see that the midplane is relatively flat in the inner galaxy, but additional encounters drive strong midplane variation. In the lower left panel, we see a strong $m = 2$ mode develop, consistent with the $R = 8$ kpc panel of Figure 17 in Laporte et al. (2018a). The lower right panel, which shows the galaxy after some relaxation has occurred is qualitatively similar to the midplane variations we saw in the FIRE simulations (Figure 6), evidence that they are at least partially driven by mergers.

4.4. Velocity Variations

We also expect that the LSR should vary as a function of azimuth. We perform this calculation in Appendix D to estimate the components of the LSR as a function of azimuth, but performing a best-fit subtraction to correct for misalignment of the original coordinate system (as in the previous section) is more involved. Since we find that the variation in the LSR is less pronounced than for the midplane, and since offsets in velocity only contribute to second order to ΔJ_R and ΔJ_z when a star is at maximum amplitude in R or z (where the majority of the orbit is, see Section 2.2), we defer this calculation to future work.

5. DISCUSSION

We have used high-resolution cosmological simulations to illustrate that we expect the “local midplane” defined by stellar density to vary with azimuth by up to ± 100 pc, as a natural consequence of the non-axisymmetry of the Galactic disk at small scales.

While this is not in itself surprising or new, we also demonstrated that extending the coordinate system established by our local midplane to a global axisymmetric coordinate system spanning the entirety of the Galactic disk introduces systematic error in computations of the actions under this symmetry assumption, when starting from the present-day positions and velocities of stars as measured by, e.g., *Gaia*.

These systematic errors are most important for stars on thin disk-like orbits, where they can be large enough to yield actions representative of orbits in the thick disk. This effect is entirely due to the extension of a local to a global coordinate system, and is separate from real diffusion in stellar integrals of motion caused by interactions with these same deviations from axisymmetry, such as

resonant perturbation by spiral arms or scattering from molecular clouds.

This finding has many implications for the study of the dynamics of stars in what is normally considered the regime of the epicyclic approximation: quasi-harmonic oscillations around a circular “guiding center orbit.”

5.1. Estimate of Milky Way Midplane Offsets from Current Data

Systematic variations in v_z were first noted as asymmetries in the local velocity distribution towards the North and South Galactic Caps from the radial velocity surveys of the Sloan Digital Sky Surveys (Widrow et al. 2012) and RAdial Velocity Experiment (Williams et al. 2013). Subsequently, Carlin et al. (2013) pointed out suggestions of an oscillation in average vertical velocities of order 5 km/s on \sim kpc scales looking toward the Galactic anticenter. Work by the *Gaia* collaboration confirmed these preliminary results on the velocity and spatial scales of these oscillation with clear spatial maps made using DR2 data of median v_z over a significant Galactic volume (Gaia Collaboration et al. 2018; Friske & Schönrich 2019). We also see in the FIRE simulation that the vertical velocity variation as a function of azimuth is ~ 5 –10 km/s (Figure 12), consistent with these observations.

The vertical frequency of the thin-disk and thick-disk orbits are $\sim 0.09 \text{ Myr}^{-1}$ and $\sim 0.06 \text{ Myr}^{-1}$, respectively. By dimensional analysis, and assuming a vertical velocity variation of 5 km/s, we therefore expect the midplane offsets to be ~ 57 –85 pc. We stress that this is a rough calculation, but it shows that already we see evidence in the data from velocities for midplane offsets on the order of what we saw in both sets of simulations.

5.2. Coordinate System Offsets

In Section 3 we discussed the current observational efforts to measure the parameters of the Galactocentric coordinate system. We noted that the solar height is discrepant between gas-based and stellar-based determinations by ~ 5 pc. While the effect is small and thus only likely to dominate the intrinsic midplane variations on small scales, it may be important for detailed modeling of kinematically cold stars where a 5 pc offset is relevant.

We also noted that the distance from the Sun to Sgr A* has been recently measured to a very low uncertainty of $\sim 0.3\%$ or ± 25 pc (Abuter et al. 2019). However, the location of Sgr A* may not be equivalent to the location of the “dynamical Galactic center,” i.e., the point in three-dimensional space about which the stars in the solar neighborhood are orbiting. This assump-

tion, although sensible and frequently made, has not yet been justified.

If the dynamical Galactic center is offset from Sgr A* by 100 pc, only a 1.2% difference, then this induces a 21% error in J_R (see Section 2.4). The reason such a large error in J_R can be generated by a small error in R_0 can be understood from the epicyclic approximation, which states that $\Delta J_R/J_R = 2\Delta R/A_R$. The fractional error in J_R is related to the error in R_0 as a fraction of the *radial amplitude* of the orbit, which is much smaller than R_0 (~ 1.2 kpc for the thin-disk and thick-disk orbits we considered). This also implies the very precise 0.3% measurement of R_0 still translates to a $\sim 4\%$ uncertainty in J_R .

The assumption that the dynamical Galactic center and Sgr A* are colocated is tested in any construction of a dynamical model where R_0 is a free parameter. For example, Küpper et al. (2015) measured R_0 while modeling the dynamics of the stream Palomar 5. Many other dynamical measurements of R_0 have been made (Bland-Hawthorn & Gerhard 2016 summarize many pre-*Gaia* results), but none have yet achieved a precision comparable to that of the distance to Sgr A*.

We did not consider in this text the effect of the *angular position* of the dynamical Galactic center being offset with Sgr A*.

6. CONCLUSIONS

Actions have promise as excellent orbit labels. If the Galaxy can be approximated as axisymmetric and 6D phase space positions can be measured accurately and precisely enough, then the computed actions are invariant with orbital phase. However, we have shown that the fact that the Galactic midplane is not constant across the disk presents a significant complication to computed actions actually being invariant. Our main conclusions are as follows:

- Inaccuracy in the Galactocentric coordinate system induces phase-dependence in the actions calculated from the observed positions and velocities of stars (Figures 1 and 2). Since stars' instantaneous phase-space positions are measured without prior knowledge of their orbital phases, this results in systematic error in the computed actions (Figure 4).
- Inaccuracy in the midplane location most severely affects computation of the vertical action J_z . A midplane offset of ~ 6 pc (~ 50 pc) for a typical thin (thick) disk orbit results in a 10% error in J_z (as defined by one half the middle 90th percentile).

The fractional error is significantly less for halo orbits.

- The distribution of systematic errors in the actions induced by a coordinate system offset is very non-Gaussian. The distribution is bimodal with *neither mode at null*. As a result, error propagation of coordinate system offsets is complex when considering actions, and is likely to significantly deform the action-space distribution function.
- Dynamical modeling across large regions of the disk, over which the midplane location varies by more than the limits discussed above, is susceptible to this type of systematic error, since the assumption that our local Galactic midplane is the global Galactic midplane is not true a priori.
- To demonstrate the previous point, we measured the local galactic midplane along the Solar circle in three different high-resolution, zoom-in simulations of Milky Way mass galaxies from the FIRE collaboration. We found that the midplane varies as a function of azimuth at the Solar circle by $\sim 185, 162, 84$ pc (middle 90%) for the three galaxies we considered (m12i, m12f, and m12m, respectively).
- Assuming a vertical velocity variation of the Milky Way of ~ 5 km/s, consistent with recent results from *Gaia* DR2 (Gaia Collaboration et al. 2018; Friske & Schönrich 2019) and our results from the FIRE simulations (Figure 12), we estimated that the corresponding midplane offsets are ~ 60 – 90 pc by dimensional analysis with the vertical frequencies of disk-like orbits.
- While inaccuracies in the parameters of the currently adopted Galactocentric coordinate system are likely to be unimportant for most applications, we discussed the importance of testing the assumption that the dynamical Galactic center is colocated with Sgr A*, which we mentioned how to do.
- This work emphasizes the importance of combining chemistry and dynamics. Chemical tagging (Freeman & Bland-Hawthorn 2002) and dynamical tagging must complement and confirm each other. The importance of combining chemistry and dynamics for Galactic archaeology was recently pointed out by Kamdar et al. (2019).
- While in this work we have focused on systematic errors in action computation, all of our conclusions

also extend to studies of stars that simply rely on orbit integration, since the computation of actions and orbit integrations are mathematically equivalent.

Our main point is that the local midplane varies between different points in the Galaxy, and that this variation can lead to significant systematic errors in the computation of actions under the assumption of a global axisymmetric potential. We do not propose here what a modeler should use for the “true” global midplane, since it depends on the particular problem being studied. Even without a high-precision definition of the global Galactic midplane, current observations from *Gaia* should soon permit a measurement of the real azimuthal dependence of the midplane location. For some applications, such as those using actions as labels to group stars on similar orbits, using such a measurement to shift stars to a consistent midplane height as a function of azimuth before using a global axisymmetric approximation to the potential may be sufficient, although this ignores the *dynamical* implications of shifts in the midplane height (which result from fluctuations in the local density). However, for other applications, such as

the study of action diffusion which motivated this paper in the first place, a more extensive perturbative approach is likely to be needed. We plan to explore the mitigation of these effects in future work.

We would like to thank Megan Bedell, Robert A. Benjamin, Tobias Buck, Elena D’Onghia, Benoit Famaey, and Adrian Price-Whelan for helpful discussions. A.B. would like to thank Todd Phillips for helpful discussions. A.B. was supported in part by the Roy & Diana Vagelos Program in the Molecular Life Sciences and the Roy & Diana Vagelos Challenge Award. K.V.J.’s work was performed in part during the Gaia19 workshop and the 2019 Santa Barbara Gaia Sprint (also supported by the Heising-Simons Foundation), both hosted by the Kavli Institute for Theoretical Physics at the University of California, Santa Barbara. K.V.J.’s contributions were supported in part by the National Science Foundation under grants NSF PHY-1748958 and NSF AST-1614743. M.-M.M.L. was partly supported by NSF grant AST18-15461. The work of D.A.-A., A.B., D.W.H., C.F.P.L., R.S., K.V.J., M.-M.M.L., and M.K.N. is supported by the Simons Foundation.

APPENDIX

A. ORBITS

We plot the three orbits considered throughout the work (Table 1) in Figure 8.

B. ΔR - ΔX RELATION

We considered the effect on actions of an inaccuracy in the distance from the Sun to the Galactic center, which introduces an offset in the x coordinate, Δx , of each star when converting to a Galactocentric coordinate system. In observations of nearby stars, we have that $\Delta x \sim \Delta R$. However, for the experiment we performed in Section 2.4 we considered observations of a star throughout its entire orbit. Therefore, we must average ΔR over the course of the orbit. We derive this relation now.

An offset Δx results in an erroneous radius R_{err} related by the formula,

$$(x + \Delta x)^2 + y^2 = R_{\text{err}}^2. \quad (\text{B1})$$

Keeping only terms to first order in Δx , we have that,

$$\begin{aligned} R_{\text{err}}^2 &= R^2 - 2R \cos \phi \Delta x \\ \implies \Delta R &\equiv |R_{\text{err}} - R| = |\cos \phi| \Delta x. \end{aligned} \quad (\text{B2})$$

Averaging over the circle, we therefore have that,

$$\langle \Delta R \rangle = \frac{2}{\pi} \Delta x. \quad (\text{B3})$$

C. J_R AND J_ϕ OBSERVED DISTRIBUTIONS

In Figure 9 we plot the observed J_R distribution induced by an offset in z , and in Figures 10 and 11 we plot the observed J_R and J_ϕ distributions induced by an offset in x . We plot the distributions for the thick-disk (top panels) and thin-disk (bottom panels) orbits.

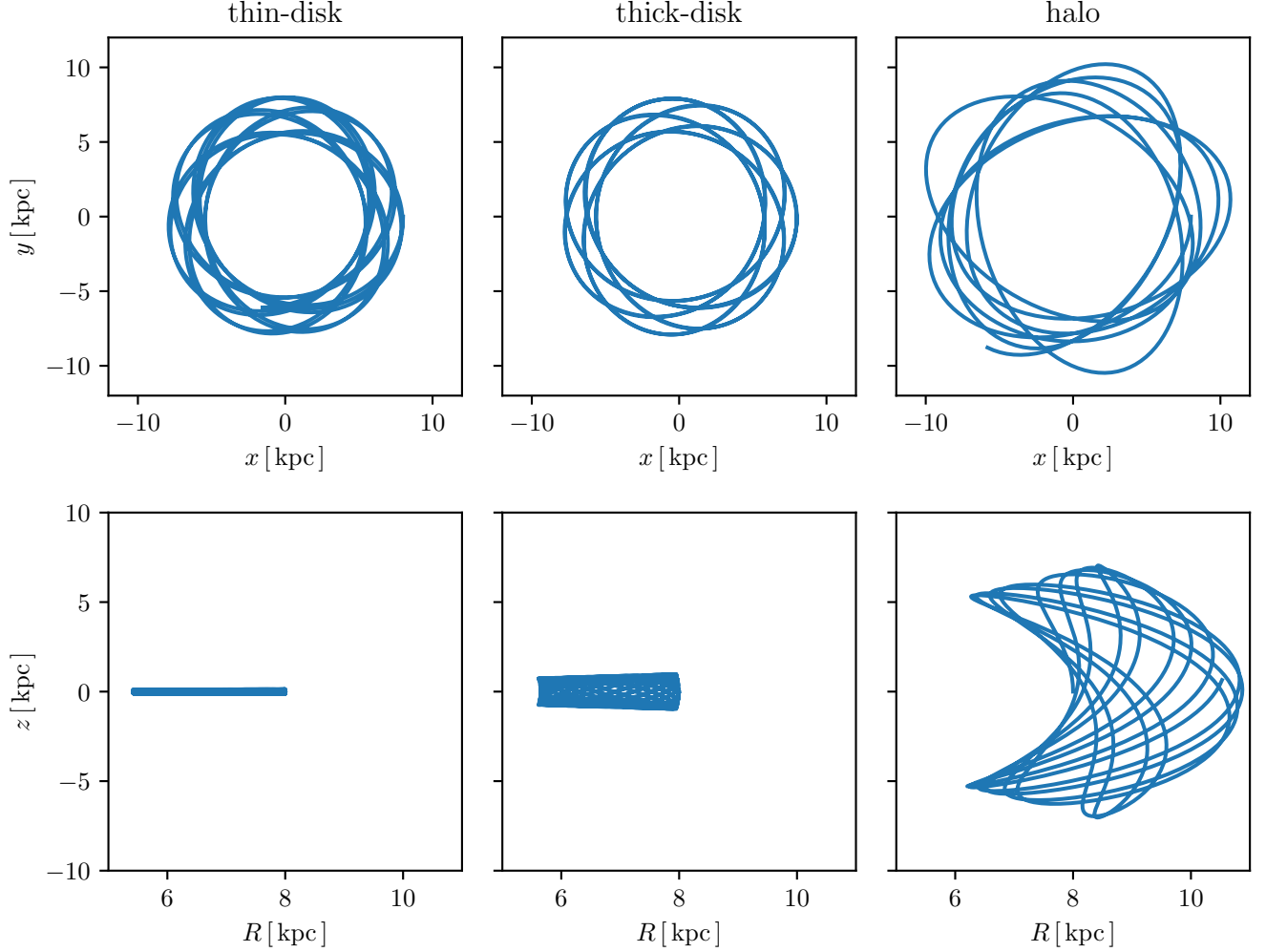


Figure 8. The three orbits presented in Table 1 and considered throughout the work. We plot the thin-disk, thick-disk, and halo orbits in the left, center, and right columns, respectively. The upper row shows a plot of x vs. y while the lower row shows R vs. z .

We find that the observed J_R distribution induced by an offset in x more closely resembles a Gaussian, while the observed J_R distribution induced by an offset in z and the observed J_ϕ distribution induced by an offset in x are both similar to the observed J_z distribution induced by an offset in z (see Figure 3).

D. LSR VARIATIONS

We consider the variations of the LSR as a function of azimuth at the fiducial solar circle ($R_0 = 8.2$ kpc) in Figure 12. At each azimuth, ϕ , we take the median velocity in cylindrical coordinates of all stars within 200 pc of the position, following Sanderson et al. (2018). No best-fit subtraction was performed as in Figure 6.

REFERENCES

- | | |
|--|--|
| Abuter, R., Amorim, A., Bauboeck, M., et al. 2019, arXiv e-prints, arXiv:1904.05721. | Anderson, L. D., Wenger, T. V., Armentrout, W. P., |
| https://arxiv.org/abs/1904.05721 | Balser, D. S., & Bania, T. M. 2019, ApJ, 871, 145, |
| | doi: 10.3847/1538-4357/aaf571 |

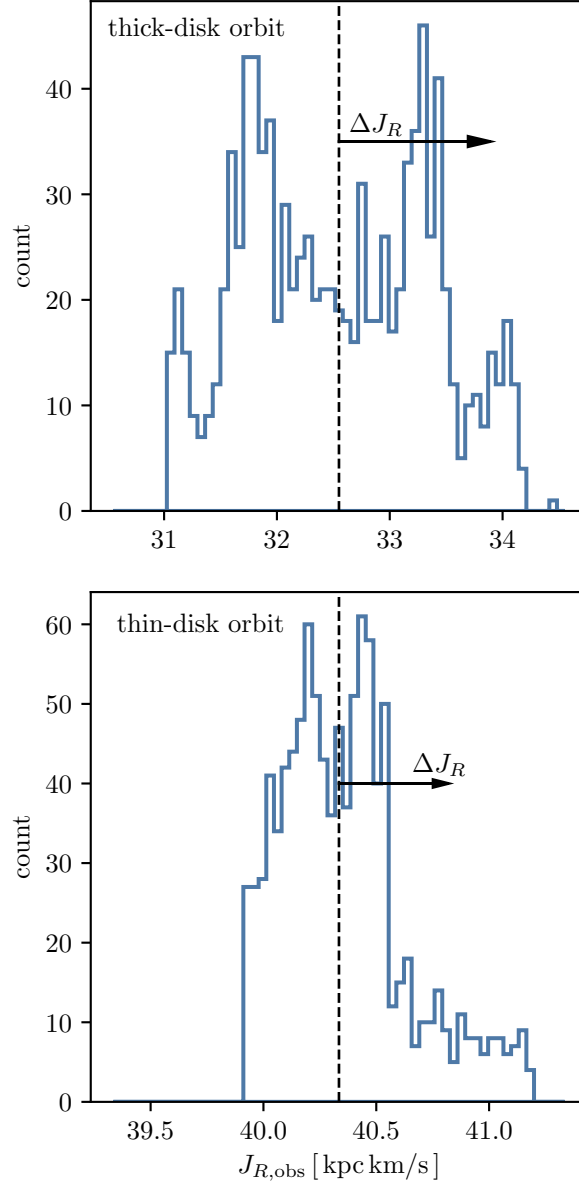


Figure 9. A histogram of the observed values in J_R for the thick-disk (top panel) and thin-disk (bottom panel) orbits assuming a z offset of 100 pc. The induced error distribution more closely resembles a Gaussian centered on the null value.

Anglés-Alcázar, D., Faucher-Giguère, C.-A., Kereš, D., et al. 2017, MNRAS, 470, 4698, doi: [10.1093/mnras/stx1517](https://doi.org/10.1093/mnras/stx1517)

Antoja, T., Helmi, A., Romero-Gómez, M., et al. 2018, Nature, 561, 360, doi: [10.1038/s41586-018-0510-7](https://doi.org/10.1038/s41586-018-0510-7)

Beane, A., Ness, M. K., & Bedell, M. 2018, ApJ, 867, 31, doi: [10.3847/1538-4357/aae07f](https://doi.org/10.3847/1538-4357/aae07f)

Bennett, M., & Bovy, J. 2019, MNRAS, 482, 1417, doi: [10.1093/mnras/sty2813](https://doi.org/10.1093/mnras/sty2813)

Binney, J. 2012, MNRAS, 426, 1324, doi: [10.1111/j.1365-2966.2012.21757.x](https://doi.org/10.1111/j.1365-2966.2012.21757.x)

Binney, J., & Schönrich, R. 2018, MNRAS, 481, 1501, doi: [10.1093/mnras/sty2378](https://doi.org/10.1093/mnras/sty2378)

Binney, J., & Tremaine, S. 2008, Galactic Dynamics: Second Edition (Princeton University Press)

Blaauw, A., Gum, C. S., Pawsey, J. L., & Westerhout, G. 1960, MNRAS, 121, 123, doi: [10.1093/mnras/121.2.123](https://doi.org/10.1093/mnras/121.2.123)

Bland-Hawthorn, J., & Gerhard, O. 2016, ARA&A, 54, 529, doi: [10.1146/annurev-astro-081915-023441](https://doi.org/10.1146/annurev-astro-081915-023441)

Bland-Hawthorn, J., Sharma, S., Tepper-Garcia, T., et al. 2019, MNRAS, 486, 1167, doi: [10.1093/mnras/stz217](https://doi.org/10.1093/mnras/stz217)

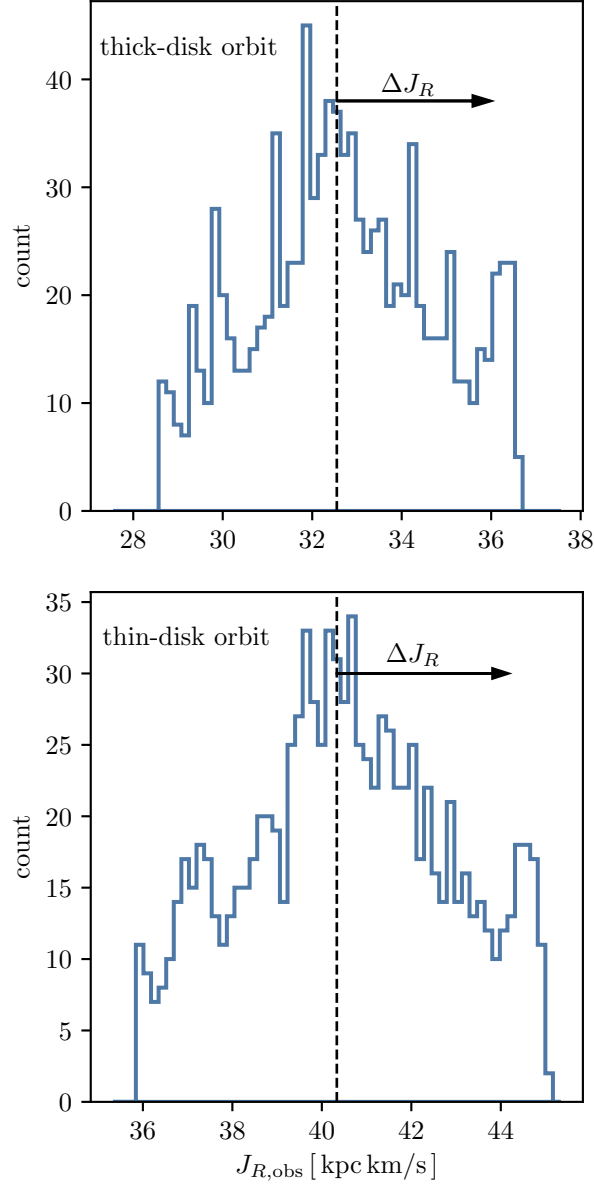


Figure 10. A histogram of the observed values in J_R for the thick-disk (top panel) and thin-disk (bottom panel) orbits assuming a x offset of 100 pc. The induced error distribution is non-Gaussian and bimodal, with neither of the modes centered on null.

Bonaca, A., Hogg, D. W., Price-Whelan, A. M., & Conroy, C. 2018, ArXiv e-prints.

<https://arxiv.org/abs/1811.03631>

Bovy, J. 2015, The Astrophysical Journal Supplement Series, 216, 29, doi: [10.1088/0067-0049/216/2/29](https://doi.org/10.1088/0067-0049/216/2/29)

Bovy, J., Allende Prieto, C., Beers, T. C., et al. 2012, ApJ, 759, 131, doi: [10.1088/0004-637X/759/2/131](https://doi.org/10.1088/0004-637X/759/2/131)

Carlin, J. L., DeLaunay, J., Newberg, H. J., et al. 2013, ApJ, 777, L5, doi: [10.1088/2041-8205/777/1/L5](https://doi.org/10.1088/2041-8205/777/1/L5)

Chen, B., Stoughton, C., Smith, J. A., et al. 2001, ApJ, 553, 184, doi: [10.1086/320647](https://doi.org/10.1086/320647)

Das, P., Hawkins, K., & Jofre, P. 2019, arXiv e-prints, arXiv:1903.09320. <https://arxiv.org/abs/1903.09320>

de Zeeuw, T. 1985, MNRAS, 216, 273, doi: [10.1093/mnras/216.2.273](https://doi.org/10.1093/mnras/216.2.273)

Dormand, J., & Prince, P. 1980, Journal of Computational and Applied Mathematics, 6, 19, doi: [https://doi.org/10.1016/0771-050X\(80\)90013-3](https://doi.org/10.1016/0771-050X(80)90013-3)

Freeman, K., & Bland-Hawthorn, J. 2002, ARA&A, 40, 487, doi: [10.1146/annurev.astro.40.060401.093840](https://doi.org/10.1146/annurev.astro.40.060401.093840)

Friske, J., & Schönrich, R. 2019, arXiv e-prints. <https://arxiv.org/abs/1902.09569>

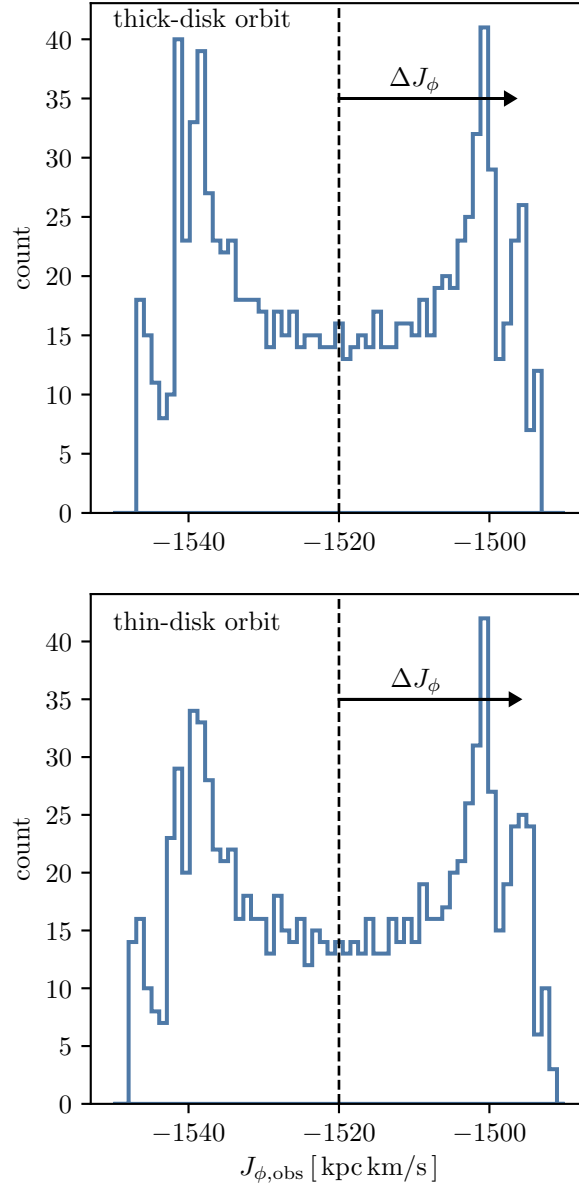


Figure 11. A histogram of the observed values in J_{ϕ} for the thick-disk (top panel) and thin-disk (bottom panel) orbits assuming a z offset of 100 pc. The induced error distribution is non-Gaussian and bimodal, with neither of the modes centered on null.

Gaia Collaboration, Katz, D., Antoja, T., et al. 2018, *A&A*, 616, A11, doi: [10.1051/0004-6361/201832865](https://doi.org/10.1051/0004-6361/201832865)

Gandhi, S. S., & Ness, M. K. 2019, arXiv e-prints, arXiv:1903.04030. <https://arxiv.org/abs/1903.04030>

Garrison-Kimmel, S., Hopkins, P. F., Wetzel, A., et al. 2018, *MNRAS*, 481, 4133, doi: [10.1093/mnras/sty2513](https://doi.org/10.1093/mnras/sty2513)

Gillessen, S., Eisenhauer, F., Trippe, S., et al. 2009, *ApJ*, 692, 1075, doi: [10.1088/0004-637X/692/2/1075](https://doi.org/10.1088/0004-637X/692/2/1075)

Goodman, A. A., Alves, J., Beaumont, C. N., et al. 2014, *ApJ*, 797, 53, doi: [10.1088/0004-637X/797/1/53](https://doi.org/10.1088/0004-637X/797/1/53)

Gravity Collaboration, Abuter, R., Amorim, A., et al. 2018, *A&A*, 615, L15, doi: [10.1051/0004-6361/201833718](https://doi.org/10.1051/0004-6361/201833718)

Helmi, A., Babusiaux, C., Koppelman, H. H., et al. 2018, *Nature*, 563, 85, doi: [10.1038/s41586-018-0625-x](https://doi.org/10.1038/s41586-018-0625-x)

Hernquist, L. 1990, *ApJ*, 356, 359, doi: [10.1086/168845](https://doi.org/10.1086/168845)

Hopkins, P. F., Kereš, D., Oñorbe, J., et al. 2014, *MNRAS*, 445, 581, doi: [10.1093/mnras/stu1738](https://doi.org/10.1093/mnras/stu1738)

Hopkins, P. F., Wetzel, A., Kereš, D., et al. 2018, *MNRAS*, 480, 800, doi: [10.1093/mnras/sty1690](https://doi.org/10.1093/mnras/sty1690)

Jeans, J. H. 1915, *MNRAS*, 76, 70, doi: [10.1093/mnras/76.2.70](https://doi.org/10.1093/mnras/76.2.70)

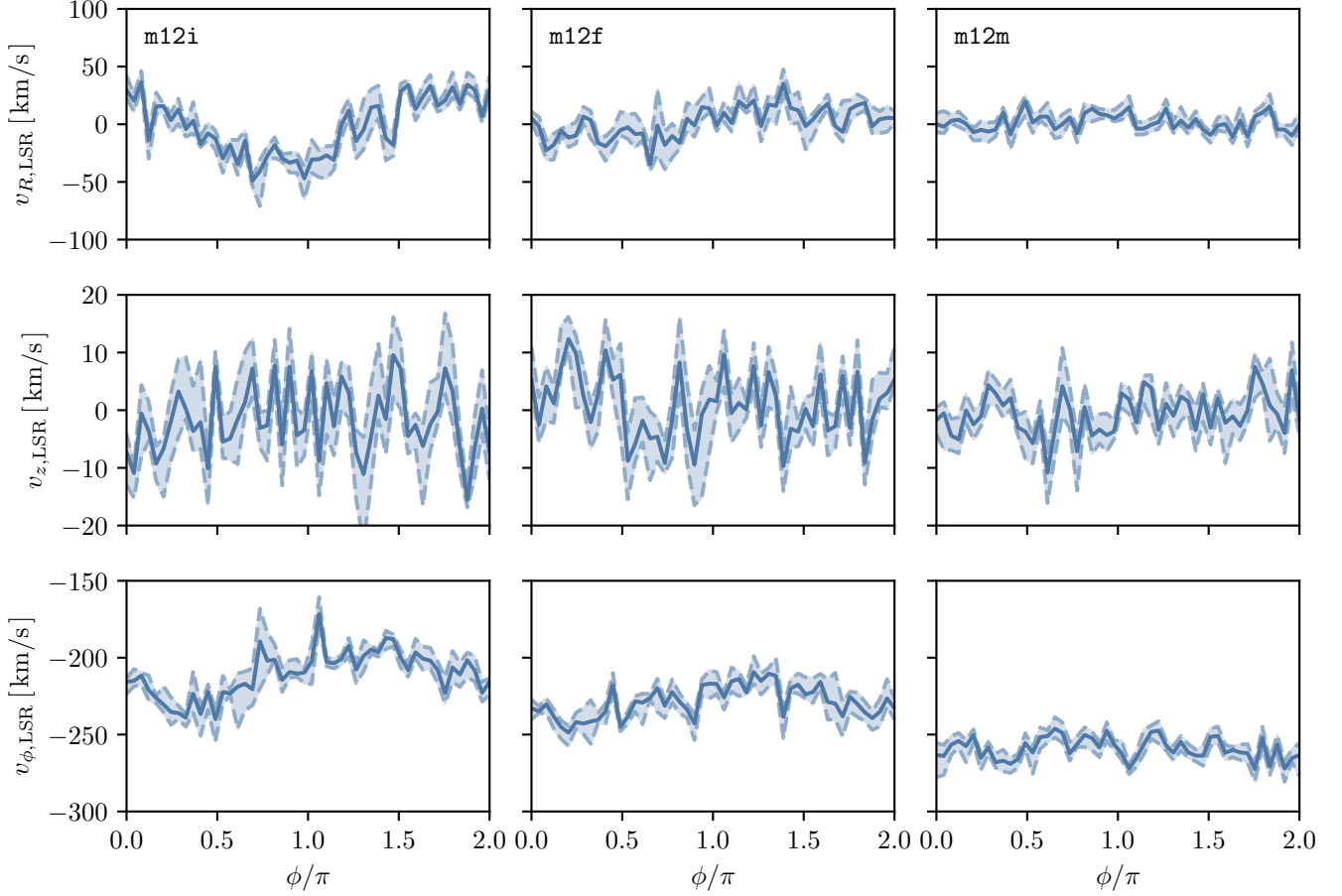


Figure 12. The LSR as a function of azimuth at the fiducial Solar circle ($R_0 = 8.2$ kpc). No best-fit subtraction is performed here as we did in the case of the midplane (Section 4.3). Variations in v_z are on the order of ~ 5 – 10 km/s.

Jurić, M., Ivezić, Ž., Brooks, A., et al. 2008, *ApJ*, 673, 864, doi: [10.1086/523619](https://doi.org/10.1086/523619)

Kamdar, H., Conroy, C., Ting, Y.-S., et al. 2019, arXiv e-prints. <https://arxiv.org/abs/1902.10719>

Katz, N., & White, S. D. M. 1993, *ApJ*, 412, 455, doi: [10.1086/172935](https://doi.org/10.1086/172935)

Khoperskov, S., Di Matteo, P., Gerhard, O., et al. 2018, arXiv e-prints. <https://arxiv.org/abs/1811.09205>

Koppelman, H., Helmi, A., & Veljanoski, J. 2018, *ApJL*, 860, L11, doi: [10.3847/2041-8213/aac882](https://doi.org/10.3847/2041-8213/aac882)

Küpper, A. H. W., Balbinot, E., Bonaca, A., et al. 2015, *ApJ*, 803, 80, doi: [10.1088/0004-637X/803/2/80](https://doi.org/10.1088/0004-637X/803/2/80)

Lancaster, L., Koposov, S. E., Belokurov, V., Evans, N. W., & Deason, A. J. 2018, arXiv e-prints. <https://arxiv.org/abs/1807.04290>

Laporte, C. F. P., Johnston, K. V., Gómez, F. A., Garavito-Camargo, N., & Besla, G. 2018a, *MNRAS*, 481, 286, doi: [10.1093/mnras/sty1574](https://doi.org/10.1093/mnras/sty1574)

Laporte, C. F. P., Minchev, I., Johnston, K. V., & Gómez, F. A. 2018b, arXiv e-prints.

<https://arxiv.org/abs/1808.00451>

Ma, X., Hopkins, P. F., Faucher-Giguère, C.-A., et al. 2016, *MNRAS*, 456, 2140, doi: [10.1093/mnras/stv2659](https://doi.org/10.1093/mnras/stv2659)

Ma, X., Hopkins, P. F., Wetzel, A. R., et al. 2017, *MNRAS*, 467, 2430, doi: [10.1093/mnras/stx273](https://doi.org/10.1093/mnras/stx273)

Mackereth, J. T., Schiavon, R. P., Pfeffer, J., et al. 2019, *MNRAS*, 482, 3426, doi: [10.1093/mnras/sty2955](https://doi.org/10.1093/mnras/sty2955)

McGill, C., & Binney, J. 1990, *MNRAS*, 244, 634

McMillan, P. J. 2017, *MNRAS*, 465, 76, doi: [10.1093/mnras/stw2759](https://doi.org/10.1093/mnras/stw2759)

Miyamoto, M., & Nagai, R. 1975, *Publications of the Astronomical Society of Japan*, 27, 533

Muratov, A. L., Kereš, D., Faucher-Giguère, C.-A., et al. 2015, *MNRAS*, 454, 2691, doi: [10.1093/mnras/stv2126](https://doi.org/10.1093/mnras/stv2126)

Navarro, J. F., Frenk, C. S., & White, S. D. M. 1997, *ApJ*, 490, 493, doi: [10.1086/304888](https://doi.org/10.1086/304888)

- Oñorbe, J., Garrison-Kimmel, S., Maller, A. H., et al. 2014, MNRAS, 437, 1894, doi: [10.1093/mnras/stt2020](https://doi.org/10.1093/mnras/stt2020)
- Price-Whelan, A., Sipocz, B., Lenz, D., Major, S., & Oh, S. 2018, adrn/gala: v0.3, doi: [10.5281/zenodo.1227457](https://doi.org/10.5281/zenodo.1227457).
<https://doi.org/10.5281/zenodo.1227457>
- Price-Whelan, A. M. 2017, The Journal of Open Source Software, 2, 388, doi: [10.21105/joss.00388](https://doi.org/10.21105/joss.00388)
- Price-Whelan, A. M., & Bonaca, A. 2018, ApJL, 863, L20, doi: [10.3847/2041-8213/aad7b5](https://doi.org/10.3847/2041-8213/aad7b5)
- Reid, M. J., & Brunthaler, A. 2004, ApJ, 616, 872, doi: [10.1086/424960](https://doi.org/10.1086/424960)
- Sanders, J. L., & Binney, J. 2014, MNRAS, 441, 3284, doi: [10.1093/mnras/stu796](https://doi.org/10.1093/mnras/stu796)
- . 2016, MNRAS, 457, 2107, doi: [10.1093/mnras/stw106](https://doi.org/10.1093/mnras/stw106)
- Sanders, J. L., & Das, P. 2018, MNRAS, 481, 4093, doi: [10.1093/mnras/sty2490](https://doi.org/10.1093/mnras/sty2490)
- Sanderson, R. E., Wetzel, A., Loebman, S., et al. 2018, ArXiv e-prints, arXiv:1806.10564.
<https://arxiv.org/abs/1806.10564>
- Schönrich, R. 2012, MNRAS, 427, 274, doi: [10.1111/j.1365-2966.2012.21631.x](https://doi.org/10.1111/j.1365-2966.2012.21631.x)
- Schönrich, R., Binney, J., & Dehnen, W. 2010, MNRAS, 403, 1829, doi: [10.1111/j.1365-2966.2010.16253.x](https://doi.org/10.1111/j.1365-2966.2010.16253.x)
- Sellwood, J. A. 2014, Reviews of Modern Physics, 86, 1, doi: [10.1103/RevModPhys.86.1](https://doi.org/10.1103/RevModPhys.86.1)
- Sellwood, J. A., Trick, W. H., Carlberg, R. G., Coronado, J., & Rix, H.-W. 2019, MNRAS, doi: [10.1093/mnras/stz140](https://doi.org/10.1093/mnras/stz140)
- Ting, Y.-S., & Rix, H.-W. 2018, arXiv e-prints.
<https://arxiv.org/abs/1808.03278>
- Trick, W. H., Bovy, J., D’Onghia, E., & Rix, H.-W. 2017, ApJ, 839, 61, doi: [10.3847/1538-4357/aa67db](https://doi.org/10.3847/1538-4357/aa67db)
- Trick, W. H., Coronado, J., & Rix, H.-W. 2019, MNRAS, 484, 3291, doi: [10.1093/mnras/stz209](https://doi.org/10.1093/mnras/stz209)
- Villumsen, J. V., & Binney, J. 1985, ApJ, 295, 388, doi: [10.1086/163383](https://doi.org/10.1086/163383)
- Wetzel, A. R., Hopkins, P. F., Kim, J.-h., et al. 2016, ApJL, 827, L23, doi: [10.3847/2041-8205/827/2/L23](https://doi.org/10.3847/2041-8205/827/2/L23)
- Widrow, L. M., Gardner, S., Yanny, B., Dodelson, S., & Chen, H.-Y. 2012, ApJ, 750, L41, doi: [10.1088/2041-8205/750/2/L41](https://doi.org/10.1088/2041-8205/750/2/L41)
- Williams, M. E. K., Steinmetz, M., Binney, J., et al. 2013, MNRAS, 436, 101, doi: [10.1093/mnras/stt1522](https://doi.org/10.1093/mnras/stt1522)